Direct Optimization of Sonic Boom Ground Noise Via a Coupled-Adjoint Method

David L. Rodriguez[1]
CFD Research Corp., Moffett Field, CA 94035

Michael J. Aftosmis,[2] Marian Nemec,[3] Sriram Rallabhandi,[4] and Wade M. Spurlock[5]

NASA Ames Research Center, Moffett Field, CA 94035

A multidisciplinary design optimization methodology to directly minimize the ground-level noise generated by the sonic boom of a high altitude supersonic body is presented. A Cartesian Euler flow solver is coupled with an atmospheric propagation tool to create a ground-noise analysis capability. Adjoint formulations for both the flow solver and propagation tool are also coupled to compute noise sensitivities to shape variations in a highly efficient manner. A gradient-based optimizer is then used to minimize objectives that are functions of ground-level noise. Output-based mesh adaptation that is driven directly by ground-level noise is employed to automatically generate meshes during the optimization. The design method was first demonstrated on a simple axisymmetric body with few lengthwise shape variables to evaluate the efficacy and validity of the optimization scheme. This design space was found to contain two local minima. Convergence of the optimization is demonstrated from multiple starting points. In addition, the method is applied to a second example with design variable placement that is guided by the coupled adjoint solution of the first problem. The design method was then applied to a low-boom aircraft at supersonic cruise to optimize control surface deflections. Two noise minimization examples and a noise maximization are presented. All optimized designs resulted in measurable improvement in

[1] Senior Research Scientist, Computational Aerosciences Branch; david.l.rodriguez@nasa.gov, Senior Member AIAA.

[2] Aerospace Engineer, Computational Aerosciences Branch; michael.aftosmis@nasa.gov, Associate Fellow AIAA.

[3] Aerospace Engineer, Computational Aerosciences Branch; marian.nemec@nasa.gov, Senior Member AIAA.

[4] Aerospace Engineer, Computational Aerosciences Branch; sriram.rallabhandi@nasa.gov, Associate Fellow AIAA.

[5] Aerospace Engineer, Computational Aerosciences Branch; wade.m.spurlock@nasa.gov, Senior Member AIAA.

the ground-level noise objective. Surveys of the design space confirm that the optimization method is effective in finding a local optimum.

Nomenclature

$ASEL$ = A-weighted Sound Exposure Levels

B_n = Bernstein polynomial scale factor

C_L = aircraft lift coefficient

C_M = aircraft pitching moment coefficient

h = cruise altitude

J_{ns} = near-field pressure signature functional

l_{ns} = length of near-field pressure signature

L = aircraft lift force

Q = **`Cart3D`** flow solution

p = local pressure

p_∞ = freestream pressure

p_{gs} = ground-level pressure signature

p_{ns} = near-field pressure signature

R_{max} = maximum radius of an axisymmetric body

T = tessellation of an outer mold line

X = generic geometry design parameters

α = angle of attack

δ_a = aileron deflection

δ_f = flap deflection

δ_s = stabilator deflection

δ_t = T-tail deflection

I. Introduction

Recent increased commercial and national interest in overland supersonic flight has spurred tremendous progress in computational sonic boom analysis. Effective methods have been developed for near-field sampling with CFD (Computational Fluid Dynamics) tools ranging from Euler to Reynolds-averaged Navier-Stokes solvers using unstructured and structured meshes [1-6]. In particular, output-based mesh adaptation, which exploits adjoint sensitivity formulations, has proven to be an enabling technology for sufficiently accurate near-field pressure signature predictions [7, 8]. Concurrently, atmospheric propagation tools have matured to the point where ground noise can be predicted within a decibel, even for low-boom aircraft designs [9-13]. When combined, these tools provide a powerful approach (depicted in Fig. 1) for the complete ground-level noise analysis of low-boom aircraft. A CFD solver is used to compute an accurate near-field pressure signature that is far enough from the aircraft to minimize complex, three-dimensional, aircraft geometry effects. This pressure signature is then processed by an atmospheric propagation tool to compute the raw ground-level acoustic signature. Furthermore, that raw signal is then appropriately weighted to compute ground-level noise metrics which strive to represent what human beings actually hear.

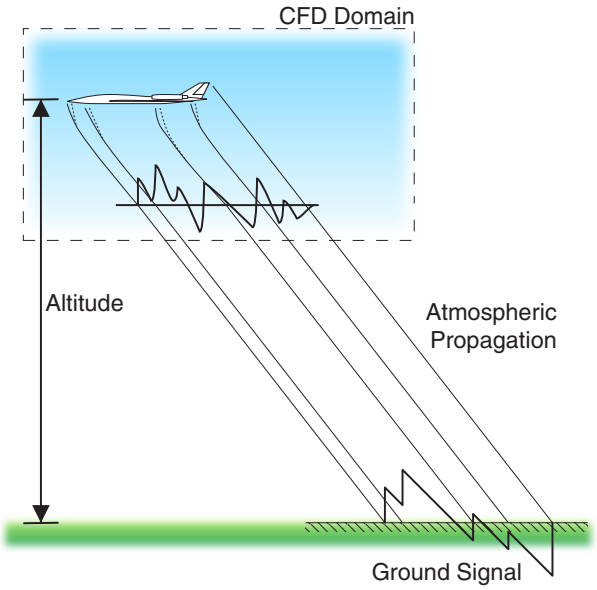


Fig. 1 Sonic boom prediction process.

While high-fidelity acoustic signature analysis has matured significantly, its applicability to design optimization has mostly been relegated to an inverse design process where the near-field pressure signature is proposed as a goal [14]. A CFD-based shape optimization method is then applied to an aircraft with the hope of actually producing this target pressure signature. While the signature is chosen so that it results in low ground noise, it can almost never be realized by an actual complex aircraft design. Likewise, an optimal target pressure signature is rarely apparent. Inverse design methods are really only productive when the optimal target is known ahead of time. Nevertheless, this technique has been shown to be effective in reducing ground-level noise of low-boom aircraft designs [14-18].

More recent work has begun to address direct minimization of ground-level noise using gradient-based methods [19]. The work presented here expands upon those efforts by detailing the latest design optimization techniques and presenting their application to two different geometries. The first application presented uses a simple axisymmetric body with a limited number of design variables, which allows the optimization results to be thoroughly validated with a detailed exploration of the design space. The second set of design problems presented involves an actual low-boom aircraft. At the time of publication, ground testing of the X-59 Quesst demonstrator [20] has begun with flight testing soon to follow. While the aircraft outer mold line is fundamentally frozen, avenues to lessen ground-level noise remain. The X-59 has four sets of control surfaces and at cruise is over-controlled, meaning that there are multiple combinations of surface deflections that allow the aircraft to maintain trimmed, level, unaccelerated flight.

The control surfaces also have an appreciable effect on the acoustic signature produced by the aircraft. This presents an opportunity to partially manage the ground-level noise of the aircraft by modifying control surface deflections and flight conditions. The design optimization tool presented in this work attempts to do just that.

II. Methodology

To directly minimize the ground-level noise produced by a body flying at high altitude and supersonic speeds, a multidisciplinary design optimization method was built using a set of already existing and well-validated tools. This set includes a parametric geometry generator, a CFD solver, an atmospheric propagation tool, and a numerical optimizer. Each tool and its role in the design method are discussed and presented below.

ESP [21, 22] is a constructive geometry creation and manipulation system specifically designed for building aerospace-related geometries. An open-source computer-aided design (CAD) geometry kernel is employed giving it the capability to output geometry files compatible with most commercial CAD packages. **ESP** can also output tessellated outer mold lines [23] which are compatible with many CFD flow solvers, a capability that is fully exploited in the presented MDO method. Parametric geometry can be built allowing the user to rapidly modify a model by simply changing the values of user-defined design parameters. Sensitivities of the geometric model to these design parameters are also exposed to the user which is an attractive feature for shape optimization. These sensitivities can also be computed for the tessellated version of the geometry model, thus making **ESP** ideal for the MDO method in particular [24].

Cart3D [25] is an aerodynamics simulation package that solves the Euler equations on an adaptive Cartesian mesh. The user provides a watertight surface triangulation, and the solver generates a Cartesian mesh automatically using the cut-cell approach [26]. The package also includes an adjoint solver [27] which allows for both output-driven mesh adaptation [28] and sensitivity calculation [29]. **Cart3D** has proven to be excellent at computing accurate near-field pressure signatures which can be used to compute the acoustic signature of a vehicle flying supersonically [30, 31]. Another tool, **trix**, is provided in the **Cart3D** package which allows the user to rotate tessellated geometry components about arbitrary axes. In this work, **trix** is used to deflect the control surfaces of an already tessellated aircraft geometry.

The third tool used to minimize ground-level noise is **sBOOM** [10], which solves an augmented Burgers equation

thus propagating a pressure signature from the cruise altitude through the atmosphere to the ground. The solver also incorporates an adjoint formulation that can compute the sensitivity of the propagated ground signature to the original pressure signature at altitude [32]. This capability is critical for both noise-driven mesh adaptation and gradient-based optimization. **sBOOM** also computes ground-level noise metrics from the ground signature, including the A-weighted Sound Exposure Level (*ASEL), BSEL*, *CSEL*, *DSEL*, *ESEL* [33, 34], and even *PLdB* [35]. Metrics like these transform the waveform of the ground signature into quantifiable measures of noise experienced by a human listener. The adjoint formulation of **sBOOM** also incorporates the noise metric computation, thus supplying the user with sensitivities of all of the noise metrics to the provided near-field pressure signature. Note that *PLdB* is a particularly sensitive metric with a derivative that is not smooth. Hence, that metric is not appropriate or reliable in a gradient-based optimization setting.

The final tool used in the MDO method is **SNOPT** [36], which uses a sequential-quadratic-programming (SQP) algorithm to perform gradient-based numerical optimization. **SNOPT** can handle both linear and nonlinear formulations of both the objective and constraints. The adjoint solvers incorporated in **Cart3D** and **sBOOM** are exploited to evaluate the gradients of any computed functions with respect to all design variables. For the direct minimization of noise from an acoustic signature, the objective function would naturally be the ground-level noise metric. Ground-level noise gradients with respect to geometry design parameters can be computed using the chain rule. For example, the gradient of *ASEL* with respect to a geometric design parameter (*X*) can be computed using Eq. (1):

$$\frac{d(ASEL)}{dX} = \frac{\partial(ASEL)}{\partial p_{gs}} \frac{\partial p_{gs}}{\partial p_{ns}} \frac{dp_{ns}}{dQ} \frac{dQ}{dT} \frac{dT}{dX} \tag{1}$$

where p_{gs} is the ground-level pressure signature, p_{ns} is the near-field pressure signature, Q is the **Cart3D** flow solution, and T is the geometry model tessellation. The gradient of *ASEL* with respect to the ground-level signature is provided by **sBOOM**, as is the gradient of the ground-level signature with respect to the near-field signature. **Cart3D** computes gradients of the near-field signature to the flow solution as well as that of the flow to the tessellation. Nemec et. al. [37] gives a detailed discussion of the **Cart3D-sBOOM** linearization. The gradient of the tessellation with respect to the design parameter is provided by **ESP** and/or **trix**.

While *ASEL* is the objective function, constraints on the forces and moments acting on the aircraft are often necessary for a realistic design problem. For example, if a constraint on the pitching moment coefficient is enforced, that gradient with respect to a geometry design parameter can be computed using Eq. (2):

$$\frac{dC_M}{dX} = \frac{\partial C_M}{\partial Q}\frac{dQ}{dT}\frac{dT}{dX} \tag{2}$$

where all of the terms are computed by **Cart3D** and perhaps **ESP** within the optimization framework [38]. For design problems involving boom propagation, exploiting cruise altitude as a design variable is often advantageous. Since **Cart3D** is an inviscid code, altitude only affects atmospheric propagation results. Theoretically, the required engine thrust should also be affected by changes in altitude, but for this work, any plume flow into a computational domain is assumed to be invariant. Doing otherwise would require introducing propulsion analysis into the design method which is currently beyond the scope of this work. Thus, **sBOOM** alone must provide gradients of the noise metric with respect to altitude (h) as in Eq. (3):

$$\frac{d(ASEL)}{dh} = \frac{\partial(ASEL)}{\partial p_{gs}}\frac{dp_{gs}}{dh} \tag{3}$$

Eq. (1) represents a fully-coupled, multidisciplinary sensitivity calculation that combines near-field CFD, atmospheric propagation, and acoustic noise evaluation. Employing this approach with the tools already described, a fully-coupled, ground-level-noise driven design optimization method can be built using the architecture shown in Fig. 2. A typical design iteration begins with predicted values for geometry design parameters (which may include body shape, control surface deflections, and/or angle of attack) provided by **SNOPT** to **ESP** and/or **trix**. The geometry is either accordingly built by **ESP** or perhaps control surfaces are deflected by **trix** to produce a new triangulation, depending on the problem being solved. **Cart3D** takes that new triangulation and generates an adapted volume mesh and solution. Forces and moments acting on the aircraft along with their gradients with respect to the design variables are fed back to **SNOPT**. The near-field pressure signature is extracted from the solution and passed to **sBOOM**. The altitude predicted by **SNOPT** is also passed to **sBOOM**. The ground pressure signature and corresponding ground-level noise metric are computed along with gradients and are passed to **SNOPT**. At that point, **SNOPT** uses the values and gradients of both the objective and constraints to determine new values for

the design variables that attempt to improve the ground noise while satisfying the constraints. Using the SQP algorithm, the process continues until a local optimum is discovered.

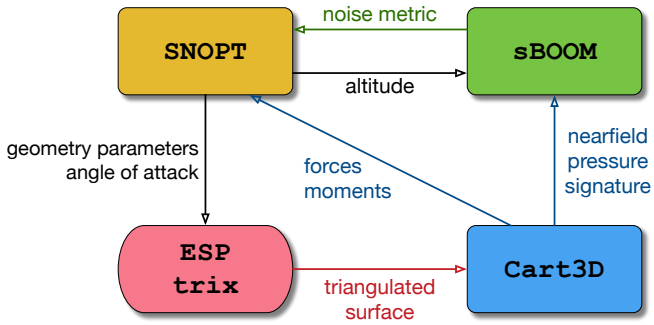


Fig. 2 Architecture of design optimization method illustrating values and their sensitivities passed between the coupled tools.

III. Applications

The methods described in the previous section were applied to two geometries: a simple axisymmetric body and the X-59 Quesst Aircraft [20] aircraft design. The simple body is used primarily to verify the method is working properly and provide a preliminary assessment of the previously described design capability. Two design problems are performed on this geometry and a thorough analysis of the results is presented. The final example represents a real-world problem: the sonic boom noise from the X-59 is reduced by identifying an optimized set of control surface deflections at cruise. The results from three design problems using this aircraft are presented.

A. Axisymmetric Body - Problem 1

The first geometry the MDO method is applied to is an axisymmetric body. The body is 200 feet long and is constrained to have a maximum radius that is no less than 5 feet. These selected dimensions were based roughly on the fuselage of a Boeing N+2 low-boom aircraft (QEVC) design [39]. Two different parameterizations of the body are presented below along with a design space analysis, optimization results, and discussion.

Lengthwise Parameterization

For this version of the problem, the geometry is constructed by first creating a baseline Sears-Haack body with a

maximum radius of 1.25 feet. Added to this thin (fixed) body are radius distributions computed by three of the five 4th-order Bernstein polynomials that have peaks at 25%, 50%, and 75% of their lengths. The two polynomials with peaks at the ends are not included since they are incompatible with the necessarily sharp nose and tail of the body. The baseline radius distribution (normalized by the constraint on maximum radius) and the raw Bernstein polynomials are shown in Fig. 3. The axisymmetric body of this problem is built by adding the radius distributions of the baseline Sears-Haack body and the Bernstein polynomials which each have a individual scale factor. In this construction, the body shape is parameterized by the scale factors for each Bernstein polynomial. An example normalized radius distribution is shown in Fig. 4. This parametrization prevents the front and back ends of the body from becoming too sharp while also permitting the axial location of the maximum radius to vary. Though the range of body shapes is ultimately limited because only three parameters can be varied, the body does lend itself to a very interesting design problem that can be easily verified.

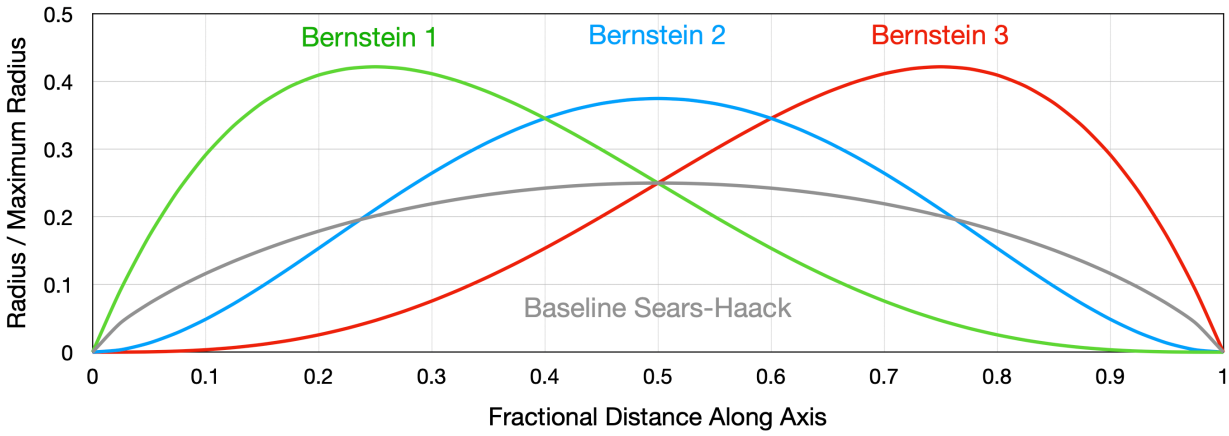


Fig. 3 Baseline radius distribution (grey) and Bernstein polynomials (green, blue, red) used to build parametrized axisymmetric body.

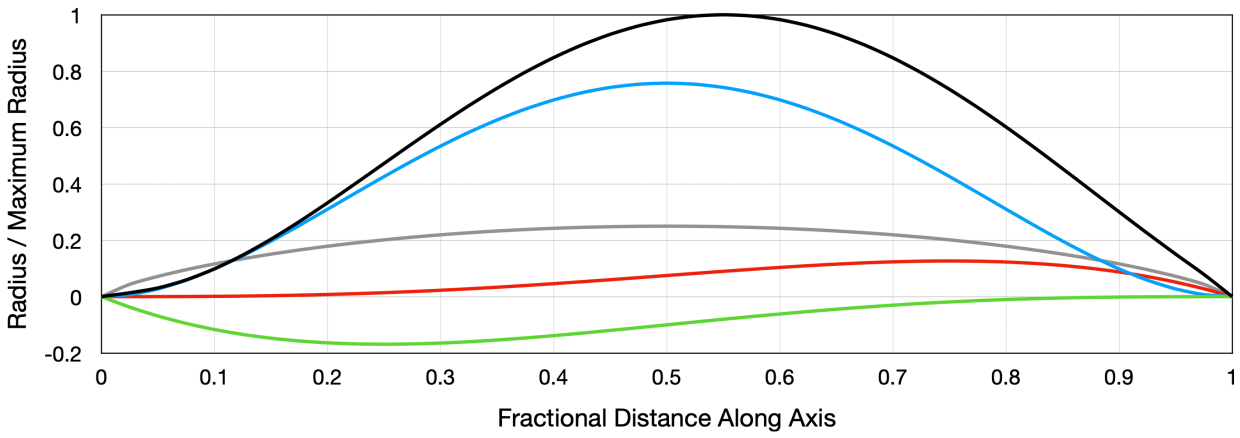


Fig. 4 Example radius distribution (black) built by superimposing the baseline shape (grey) and three individually scaled Bernstein polynomials (green, blue, red) from Fig. 3.

For this small design problem, the discrete geometric model of the body is built using **`ESP`** for any specified set of Bernstein polynomial scale factors. This parametrized body is flown at Mach 1.5 and 55,000 feet of altitude at zero angle of attack. The objective is to minimize the ground level noise produced by this geometry as measured by the *ASEL* metric. The design variables are the scale factors (designated B_1, B_2, and B_3) that are applied to the Bernstein polynomials shown in Fig. 3 to build up the body radius distribution. Eq. (4) summarizes the optimization problem:

$$\text{minimize:} \quad ASEL\,(B_1, B_2, B_3) \tag{4}$$

$$\text{subject to:} \quad R_{max} \geq 5 \text{ feet}$$

The optimization problem was solved using the MDO method presented in Fig. 2. The **`Cart3D`** meshes employed had over 100 million cells over the entire domain (no symmetry plane) and were generated using output-based adaptation. The design objective, *ASEL*, was also the functional used to drive the adaptation. A representative functional and error convergence analysis is shown in Fig. 5. The left plot shows the convergence of the functional (*ASEL*) as the mesh is adapted. The right plot shows the reduction in both the error indicator, which is used to drive the adaptation of the mesh, and the estimated error bar height surrounding the value of the functional. This error range is also shown in the functional history in the left plot as error bars. Both plots show excellent convergence of the *ASEL* functional which indicates the final value is accurate at least to about a tenth of a decibel in ASEL (dBA).

A typical final mesh generated by this analysis is shown in Fig. 6, colored by cell size.

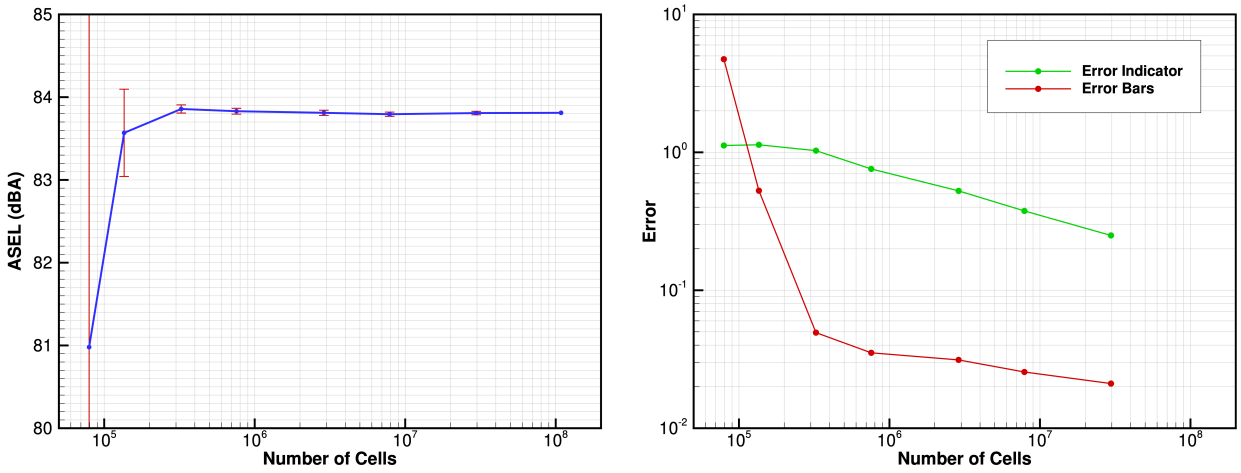


Fig. 5 Functional convergence and error reduction as the mesh is adapted for a typical analysis cycle in design of the axisymmetric body.

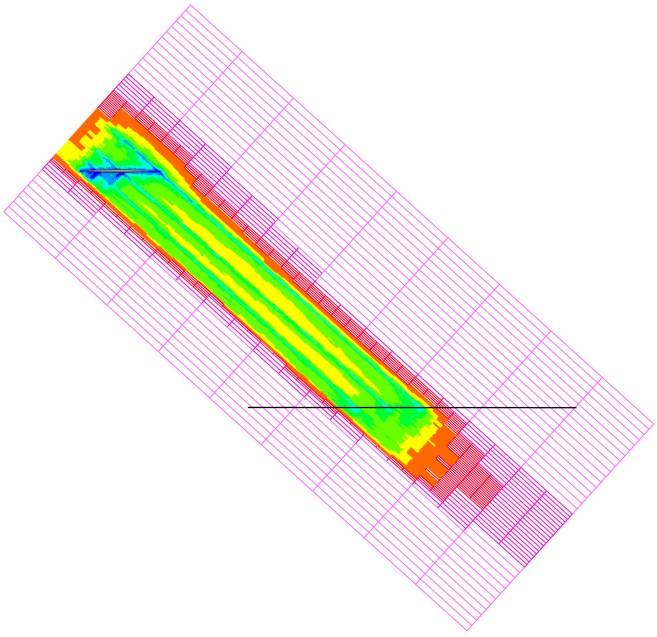


Fig. 6 Planar cut of a typical finest adapted mesh on axisymmetric body. Cells are colored by refinement level, with magenta being the coarsest and blue the finest. The body is shown in grey at the top. The nearfield pressure sensor is indicated by the black line.

In fact, the value of the functional was nearly converged after just a few adaptation cycles, but the adaptation process was continued to ensure that the design variable sensitivities, which are computed using the adjoint solution, were also sufficiently converged. Fig. 7 shows the computed gradients of *ASEL* with respect to the design variables at each adaptation cycle (mesh size). The plot shows that not all the gradients are completely converged, but they do appear to be reasonably close. The baseline geometry gradients are computed for each design variable and are represented by lines (with a single filled symbol) in Fig. 8. The neighborhood design space is also sampled and represented by open symbols in the Fig. 8 plots. Overall, the sampled design space closely matches the computed gradients. All of these results suggest that the coupling of **`Cart3D`** and **`sBOOM`** is indeed sound and could produce positive results in a gradient-based optimization setting, assuming the design space is smooth, of course.

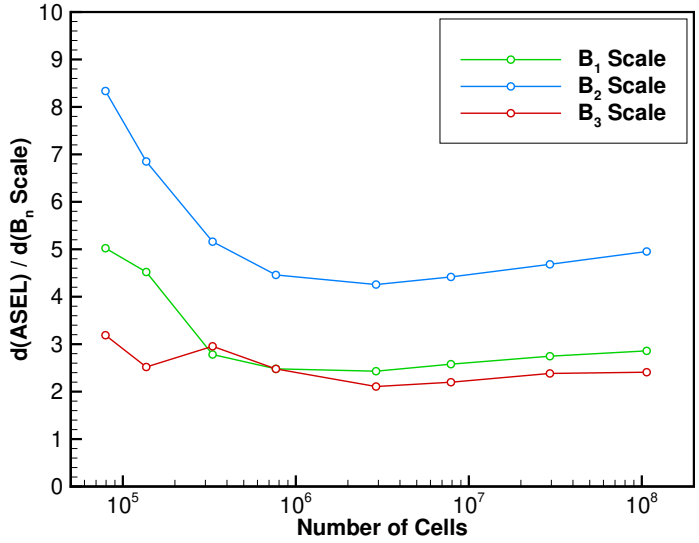


Fig. 7 Convergence of design variable gradients with adapted mesh size.

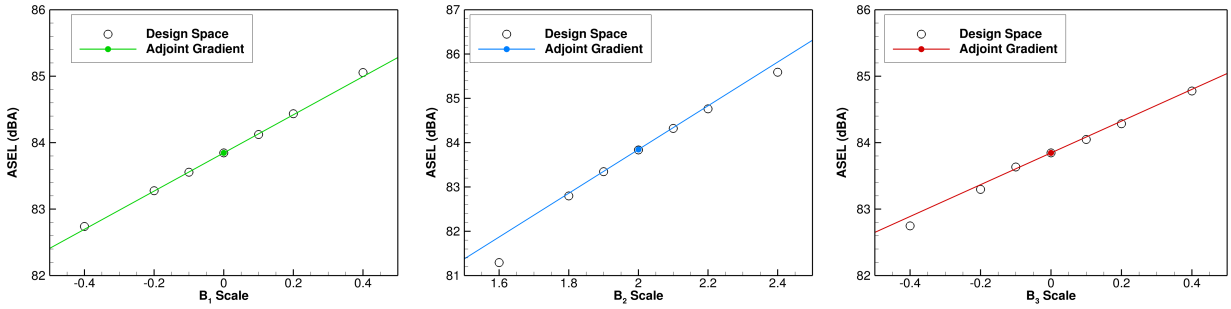


Fig. 8 *ASEL* gradients with respect to Bernstein polynomial scales as computed by coupled adjoint solver. They are compared to samplings of the actual design space.

Since this design problem has three design variables with one constraint, it is possible to make a two-dimensional plot of the constrained design space. Fig. 9 is an example of such a plot. Here, the two dimensions are the scale factors of the 1st and 3rd Bernstein polynomials (see Fig. 3). The 2nd Bernstein scale factor is constrained to whatever value gives the axisymmetric body a maximum radius of exactly 5 feet. The contours show *ASEL* values throughout this design space. Examples of the body shape are displayed in several locations of the design space for clarity. A contour plot was constructed by completing 780 analyses sampling the range of space presented. The design space is clearly multimodal. In hindsight, this is to be expected since the ground pressure signal is formed after the coalescing of multiple shocks as they propagate downward through the atmosphere. What may not have been expected is that the design space is relatively smooth. This feature should make gradient-based optimization not only possible but effective, though it certainly will not guarantee a global minimum will be found.

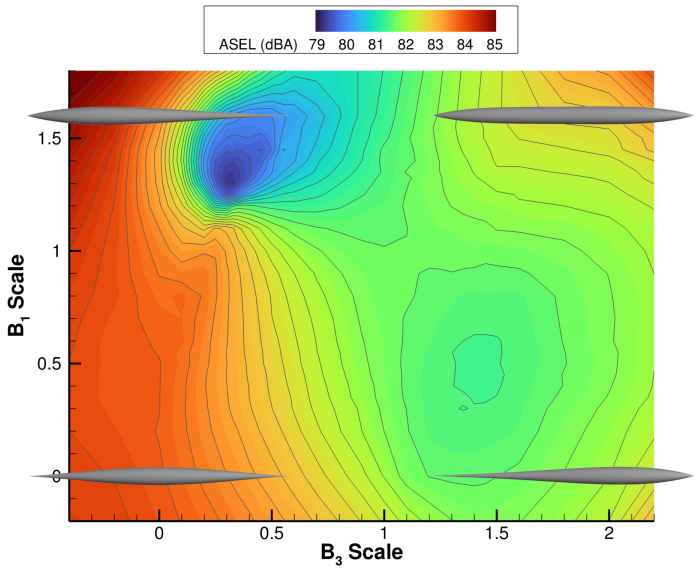


Fig. 9 *ASEL* design space of axisymmetric body, constrained in B_2 scale to match radius constraint.

After exploring the design space and verifying the gradients computed by the coupled MDO method, two optimization problems were attempted at different starting points. For the first run, the initial design started with both the B_1 and B_3 scale factors set to zero and the B_2 scale factor set to 2.0, which builds a geometry that satisfies the radius constraint exactly and is symmetric front to back. This geometry is shown as the baseline geometry in Fig. 10. The optimization history is shown in Fig. 11. The objective function (*ASEL*) is shown to be reduced to a value over 2 dBA below the initial value. The maximum radius constraint is also satisfied by reaching the constraint exactly at 5.0 feet. The optimized geometry is shown in Fig. 10. Both the nose and back end have become much blunter, and the location of the maximum radius has moved back to roughly 59% of the body length. This corresponds to the local minimum shown in Fig. 9 in the lower-right portion of the sampled design space.



Fig. 10 Baseline and optimized geometries (first run).

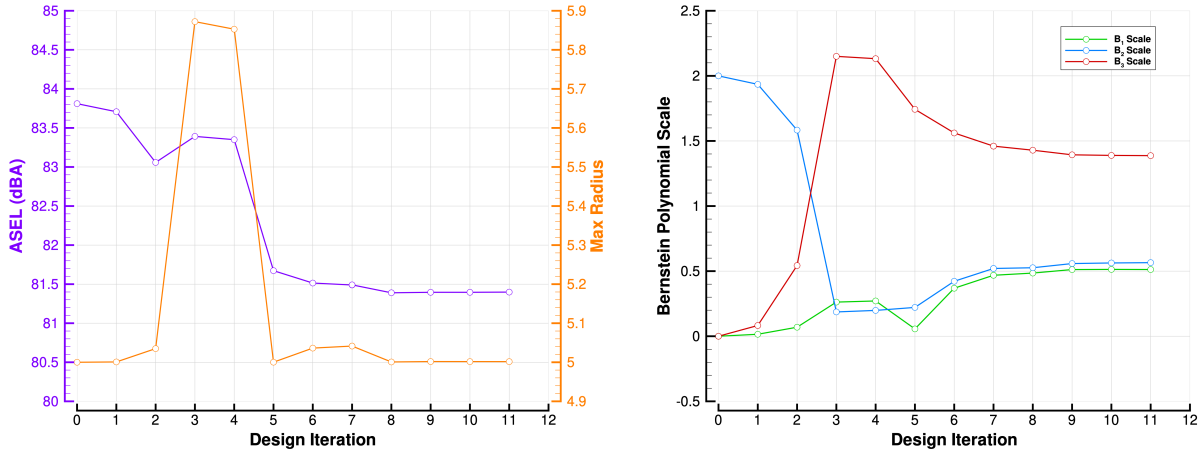


Fig. 11 Optimization history (first run) of axisymmetric body. Objective and constraint are shown on the left with the design variables on the right.

But as was revealed by Fig. 9, the design space is multi-modal; there is another local minimum that appears to be much better than this first solution. Hence, the optimization was repeated with a different starting point in hopes of driving the design to this second and indeed global minimum. The starting geometry for this problem is shown in Fig. 12. The resulting optimization history is shown in Fig. 13 indicating another optimum was found that is over 2 dBA quieter than the first optimized solution while still satisfying the constraint. The resulting optimized geometry is shown in Fig. 12, which is quite different than the optimized geometry in Fig. 10. Here the maximum radius has moved *forward* of the midpoint to roughly 37% of the body length.



Fig. 12 Baseline and optimized geometries (second run).

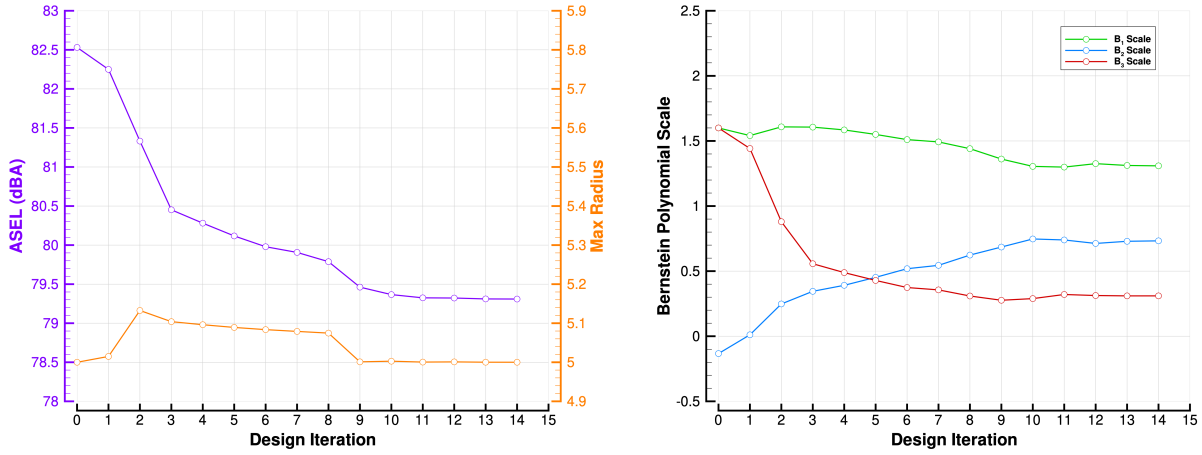


Fig. 13 Optimization history (second run) of axisymmetric body. Objective and constraint are shown on the left with the design variables on the right.

The optimization trajectories are shown in Fig. 14 as projections onto the design space of Fig. 9. Note that these trajectories do not actually lie entirely on this surface since the constraint is not satisfied at every design cycle. However, they are exactly on the surface near their ends where the optima are located. These projected trajectories behave as is expected by a constrained SQP method. Both trajectories end at or very near the optima identified in the design space sampling. These results demonstrate that the MDO method is indeed capable of locating local minima in a smooth design space. The results also show that while gradient-based optimization is possible and even effective in these types of noise minimization problems, identifying the global minimum cannot be guaranteed with just any starting point.

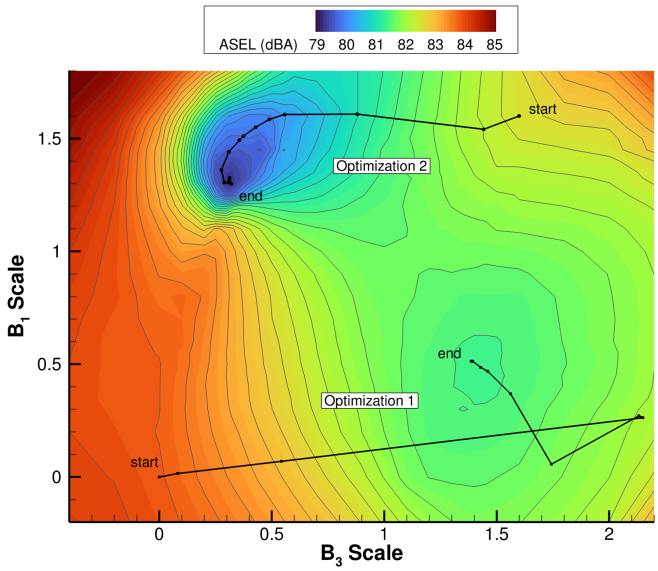


Fig. 14 Optimization trajectories projected onto constrained design space. Note the actual trajectories only lie on this surface near the optima (and starting points).

Fig. 15 shows the near-field signatures produced by both the starting and optimized geometries analyzed. Naively, one would think the signature at the start of optimization 1 (pale orange) would produce the quietest ground signal. And yet, referring back to Fig. 14, it is actually the loudest of the plotted signals. This is further evidence that prescribing a near-field pressure signature for inverse design is not straightforward.

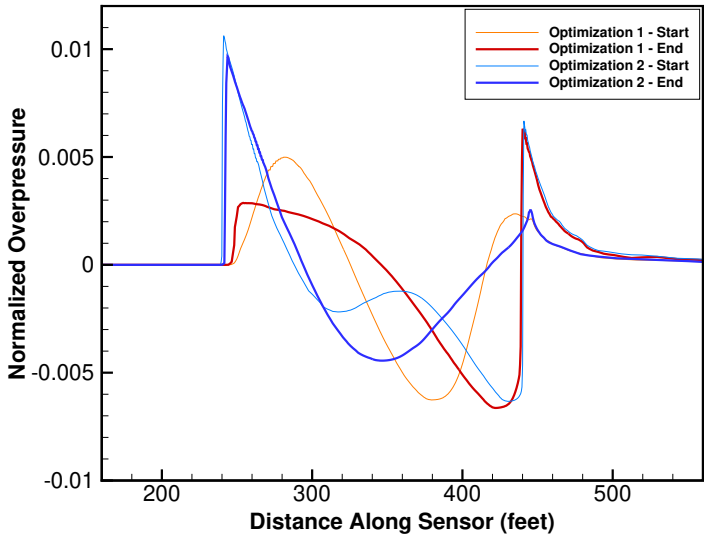


Fig. 15 Near-field pressure signatures of the starting and optimized (end) axisymmetric geometries.

The corresponding ground pressure signatures are shown in Fig. 16. The ground signatures are nearly N-waves for all geometries. The first optimized ground signature (red) has a softer and rounded peak up front along with a slightly weaker shock in the back when compared to the starting signal (pale orange). This explains the reduction in noise for the first optimization. The aft shock on the second optimized signal (blue) has a longer rise time than the starting signal (pale cyan), which explains its reduction in noise.

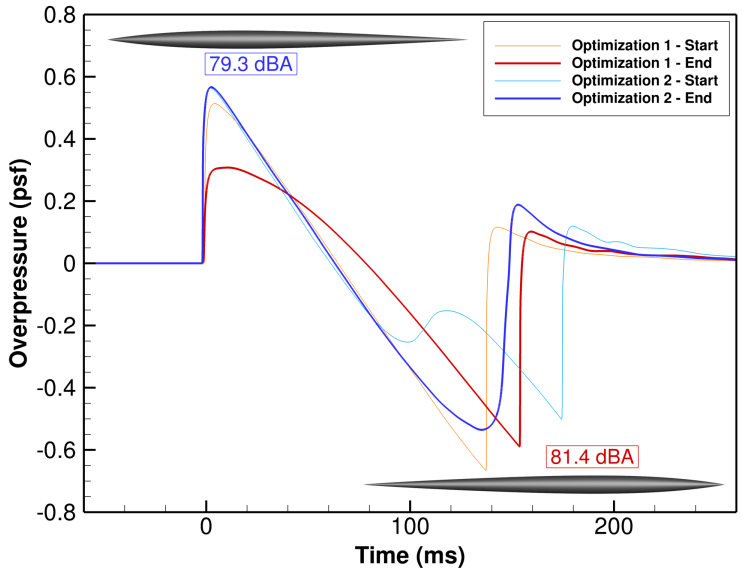


Fig. 16 Ground pressure signatures for baseline and optimized axisymmetric geometries. Optimized geometries and noise also shown.

Referring back to Fig. 16, it is not clear why the resulting noise level from the second optimization is so much lower than the first one. To explain this difference, a noise buildup analysis in both the forward and backward directions was conducted on both optimized ground pressure signals. The results are shown in Fig. 17. The backward buildup of the first optimized signal (dotted red) shows the noise is dominated by the aft shock, which is unsurprising considering the signal shape. On the other hand, the forward buildup of the second optimized signal (solid thick blue) shows that signal is dominated by the front shock, also as expected. These buildups show that the aft shock of the first optimized signal is much stronger than the forward shock of the second optimized signal. Revisiting Fig. 16, this becomes more apparent as the jump in pressure at the front shock of the second optimized signal is smaller than that of the aft shock of the first optimized signal.

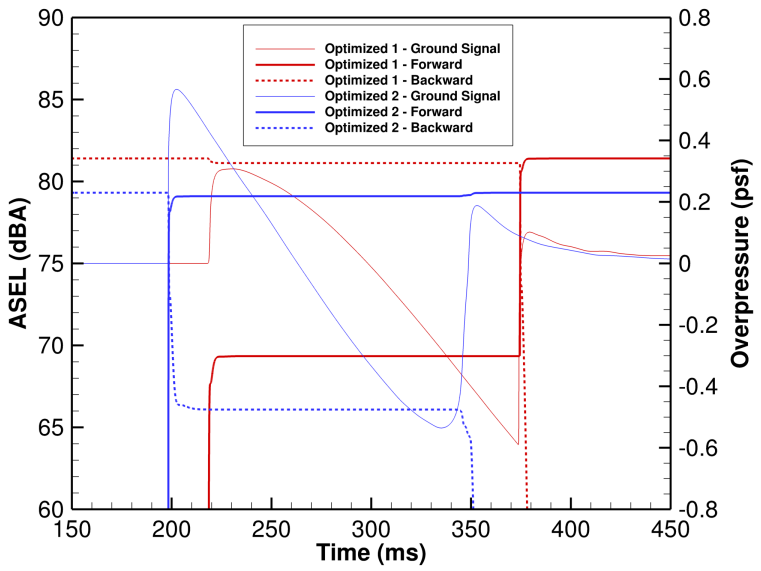


Fig. 17 Noise buildups (forward and reverse) of the optimized ground pressure signatures.

Local Bump Parameterization

A deeper dive into the previous example yields another interesting design problem. Consider the baseline symmetric geometry shown in Fig. 10. Contours of the *ASEL*-adjoint of the pressure variable on the symmetry plane are shown in Fig. 18. Note the prominent spikes in the contours that intersect at roughly 26% and 57% of the body length. Since the adjoint contours directly illustrate the sensitivity of *ASEL* noise, these indicate that the shape of the body at these limited locations should have a significant effect on the ground noise level.

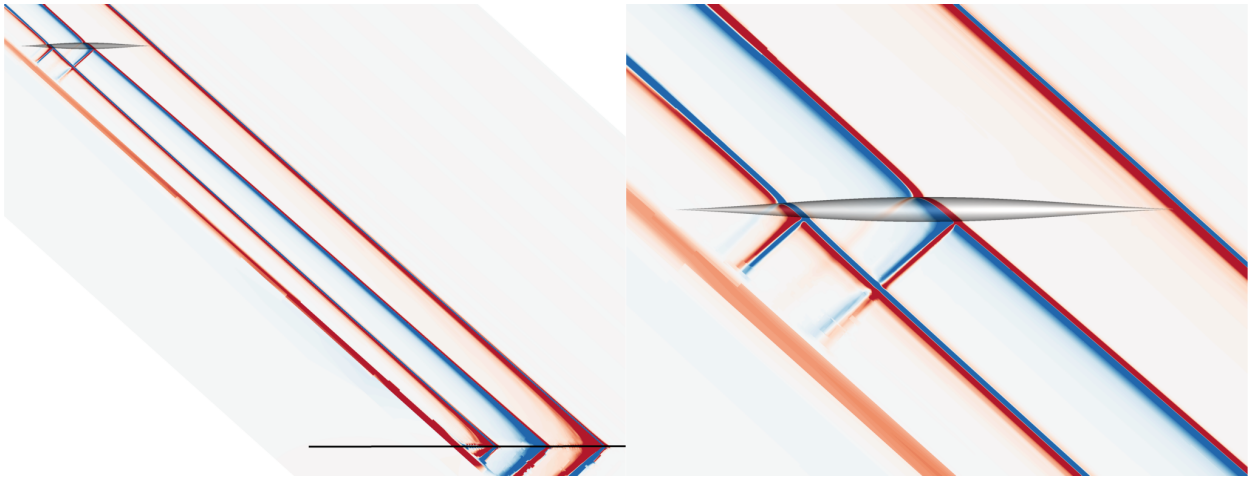


Fig. 18 Contours of pressure adjoint of *ASEL* from solution on axisymmetric body. Left image shows contours between body and line sensor (dark line). Right image is a zoom into the body itself. Intense colors represent far from zero values, while no color indicates near zero.

This observation prompted the authors to consider a second problem on the axisymmetric body. Here the baseline geometry is the same as in Fig. 10, but instead of modifying the radius distribution along the entire length of the body, only the radii at the locations of the adjoint spikes are allowed to vary. Radii in front, between, and behind these locations are held constant. Since the geometry is built by smoothly lofting a stack of circles along the length of the body, varying the radii exclusively at these locations amounts to creating small, smooth bumps or divots. Thus a new, two-variable problem is identified with no constraint necessary since the maximum radius value and location are fixed at the midsection. An example geometry with these two radii varied in an exaggerated fashion is shown in Fig. 19. Note the geometry is also scaled by a factor of two in the vertical direction for clarity.



Fig. 19 Bump/divot design variables modeled on axisymmetric body as compared to baseline (vertical scaled by 2).

The minimization of *ASEL* was repeated with changes in these two radii values as design variables (positive is a bump, negative a divot). Two different starting points were used since a prior exploration of the design space again

suggested two local minima. The results of the first optimization are shown in Fig. 20. The design problem converged rather quickly and shows a reduction in noise of less than half a decibel. The front bump scale is minuscule and the aft bump is quite small (and positive). This result suggests these bumps might not be very effective at reducing noise.

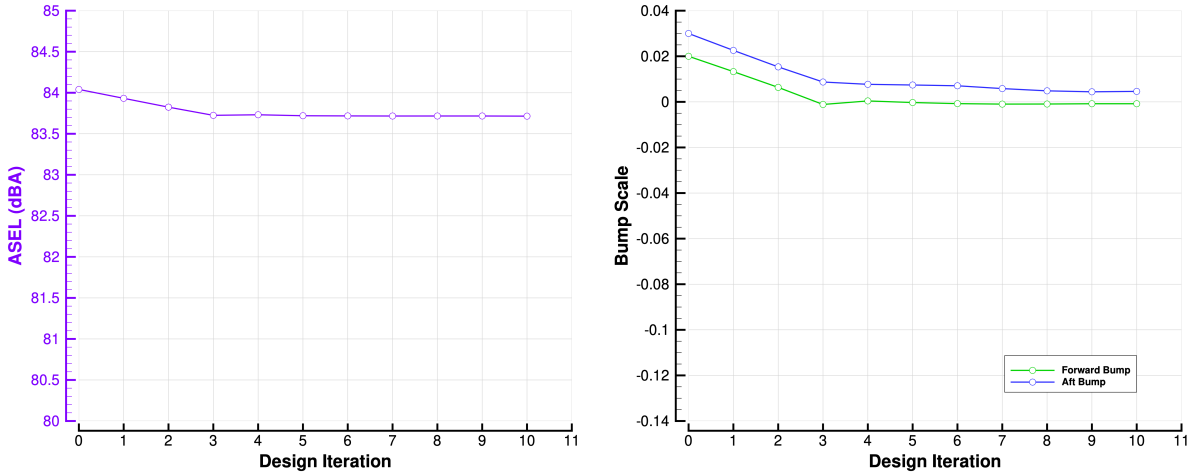


Fig. 20 Optimization history (first) of axisymmetric body with local bumps as design variables. Objective is shown on the left with the design variables on the right.

The results of the second optimization, shown in Fig. 21, are quite different. This case also converged though it took several more iterations to do so. Starting with very small divots in both locations yielded an optimized design that is well over a full decibel quieter in *ASEL*. Again the front divot is mostly zeroed out, but the aft divot has become somewhat larger than the starting divot. The final optimized geometry for this case is shown in Fig. 22, with the vertical dimension scaled by two for clarity.

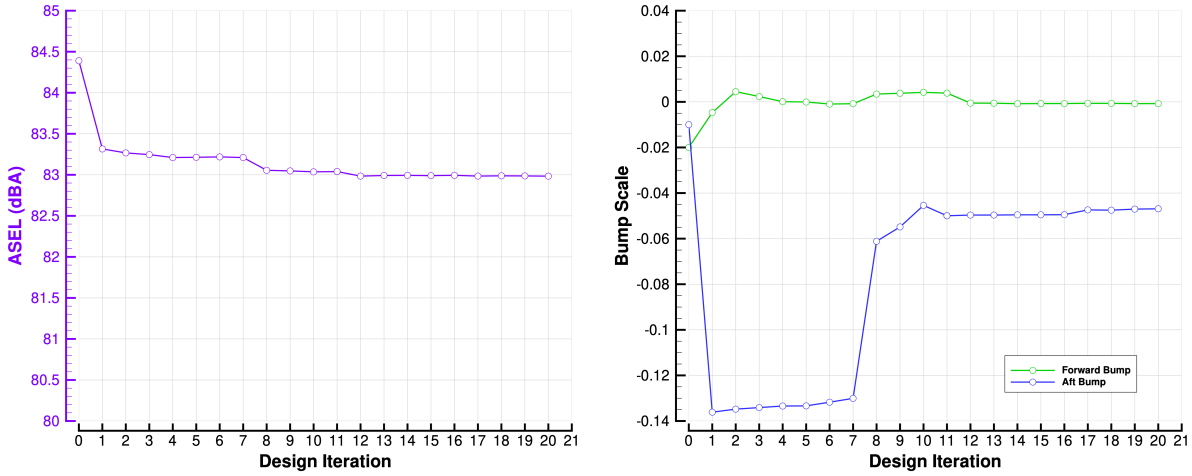


Fig. 21 Optimization history (second) of axisymmetric body with local bumps as design variables. Objective is shown on the left with the design variables on the right.



Fig. 22 Optimized axisymmetric body with bump/divot variables (second run, vertical scaled by 2).

The optimization trajectories for both designs are shown in the sampled design space plot in Fig. 23. Note that the optimizations successfully located the two local minima. The design space shows that the forward bump as parameterized is essentially optimal when it is nearly zero. The aft bump, on the other hand, clearly can be used to reduce ground noise. The ground pressure signals induced by the baseline and optimized geometries are shown in Fig. 24. The baseline is the same as the baseline signal for Optimization 1 in Fig. 16; it is essentially an N-wave. The optimized signals each show some deviation from the pure N-wave in the region in front of the second shock. These deviations are the source of noise reduction.

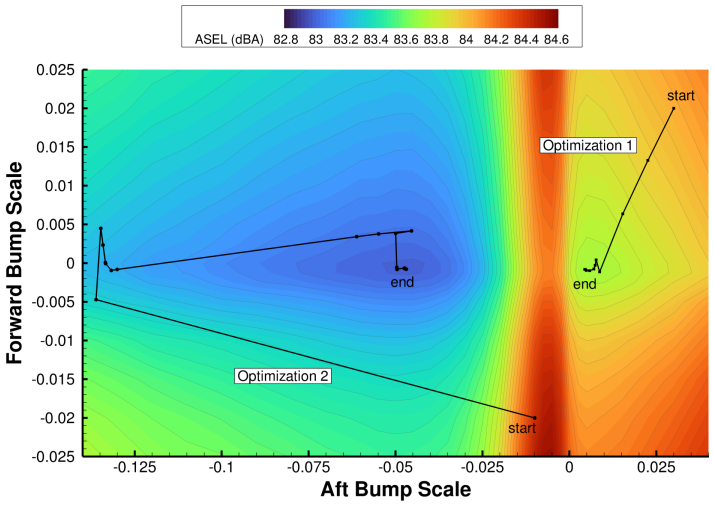


Fig. 23 Bump/divot optimization trajectories plotted in sampled design space.

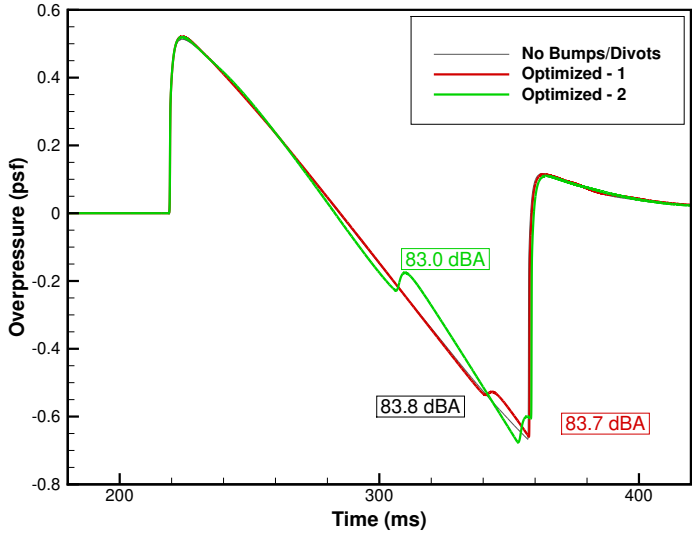


Fig. 24 Ground pressure signals from baseline and optimized bodies.

Overall, this optimization problem demonstrated that the adjoint solution produced by a ground noise based adaptation analysis can be used to identify potential design parameters. It showed that small divots on a simple axisymmetric body can have a significant effect on the ground noise. Of course, such a divot is only effective on a specific shape, at a specific Mach number, and a specific altitude. Even the aft divot probably would not be effective if the flight condition deviated from the optimized case. Such a divot would not be practical on an actual aircraft that

must be low-boom throughout its supersonic flight envelope. Nevertheless, this problem did provide another excellent example of ground-based noise minimization through shape gradient-based optimization and verified the efficacy of the design method.

B. X-59 Quesst Aircraft

The final test cases presented consider ground noise optimization of the X-59 aircraft through control surface deflections. As mentioned earlier, no changes to the outer mold line of the X-59 are possible at this time. But the aircraft is over-controlled and can fly most stable trajectories using many different settings of the control surfaces. These control surfaces are highlighted in Fig. 25. This presents an opportunity to optimize the control surface deflections for a specified objective, thus providing a real-world problem for the MDO method on a complex, low-boom aircraft design. [20]

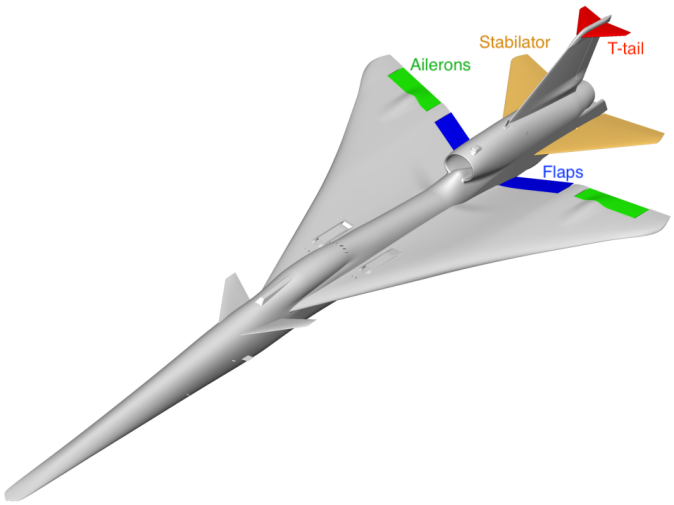


Fig. 25 X-59 aircraft with highlighted control surfaces.

Fixed Altitude with No Trim Constraint

The first and simplest problem to which the design method was applied is the direct minimization of ground-level noise at fixed altitude and lift. No trim constraints were enforced. For this design problem, the C612 revision of the X-59 was used. The optimizer varied angle of attack and all control surface deflections. Since the altitude, Mach number, and lift are constant, the lift coefficient was held fixed as a constraint. Eq. (5) summarizes the optimization problem:

$$\text{minimize:} \quad ASEL\,(\alpha, \delta_f, \delta_a, \delta_s, \delta_t) \tag{5}$$

$$\text{subject to:} \quad C_L\,(\alpha, \delta_f, \delta_a, \delta_s, \delta_t) = C_{L,cruise}$$

$$\delta_{f,min} \le \delta_f \le \delta_{f,max}$$

$$\delta_{a,min} \le \delta_a \le \delta_{a,max}$$

$$\delta_{s,min} \le \delta_s \le \delta_{s,max}$$

$$\delta_{t,min} \le \delta_t \le \delta_{t,max}$$

The bounds listed in Eq. (5) are specified in Table 1. Also listed are the initial values of the control surface deflections which are already somewhat optimized based on previous unpublished trade studies.

Table 1 Control surface deflection bounds and initial values in design optimization.

Control Surface	Minimum	Maximum	Initial
Ailerons	-3.0°	3.0°	1.1°
Flaps	-3.0°	3.0°	-1.8°
Stabilator	-15.0°	15.0°	3.2°
T-tail	0.0°	10.0°	4.3°

The optimization problem was run using the coupled design method. The computational meshes employed had roughly 140 million cells (half body) and were generated using a re-meshing capability of **`Cart3D`** to bypass mesh adaptation and speed up design cycle time. This process began by generating an original mesh for the problem using output-based mesh adaptation. The functional for this adapted mesh was based on minimizing errors in the nearfield pressure signature and is given in Eq. (6):

$$J_{ns} = \int_0^{l_{ns}} \left(\frac{p - p_\infty}{p_\infty} \right)^2 dl_{ns} \tag{6}$$

This function represents the square of the deviation from freestream pressure integrated over the length of the signal and essentially strives to minimize errors in the nearfield signature, particularly in its peaks and valleys. This adapted mesh was then used as guidance for generating all other meshes, thus matching spatial mesh refinement patterns in any new meshes. This process was appropriate for this problem since the lift coefficient is fixed and only small changes in control surface deflections were anticipated. Tiny angle of attack changes were consequently

expected and thus no significant changes in the mesh density distribution were expected to be necessary.

The results from this optimization are shown in Fig. 26. The objective function (*ASEL*) is shown to converge to a value about 0.3 dB lower than the initial value. The lift constraint also converges to the target value ($C_{L,cruise}$) designated by the dotted line. The design variable history shows that while no change in control surface deflection was substantial (all under 0.15°), the flaps and ailerons deflected the most.

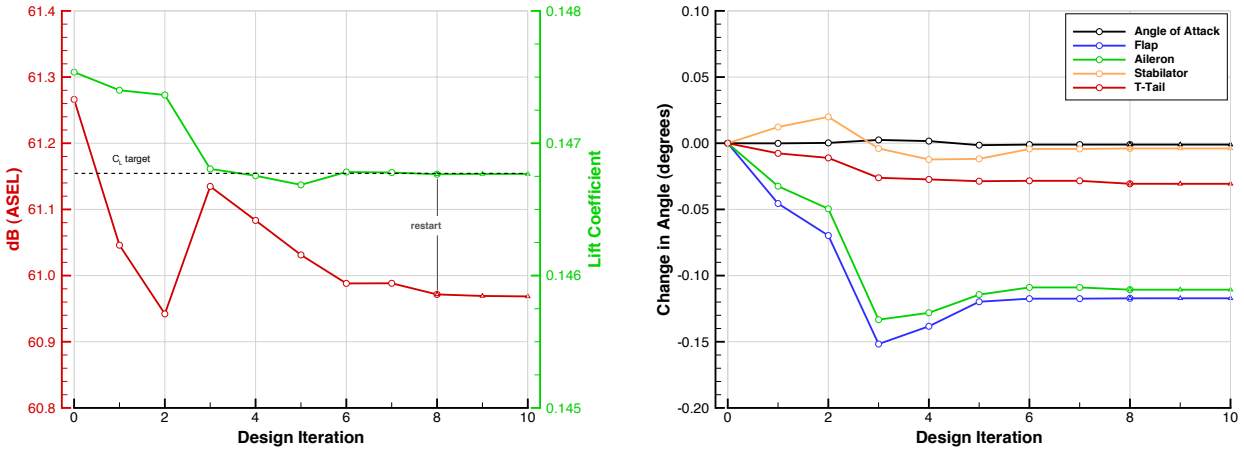


Fig. 26 Optimization history of objective (*ASEL*) and constraint (lift coefficient) in the left plot with the change in the control surface deflections in the right plot.

This relatively simple problem presented the opportunity to conduct a detailed verification of the optimization results. Thusly, the design space centered on the new optimized design was surveyed by running 80 additional analyses (9 by 9 grid). Since the flaps and ailerons deflected the most from the baseline, the first survey was conducted on the subspace where only the flaps and ailerons vary. The results of this survey are shown in Fig. 27. Note that the new optimized design is located at the origin of this plot.

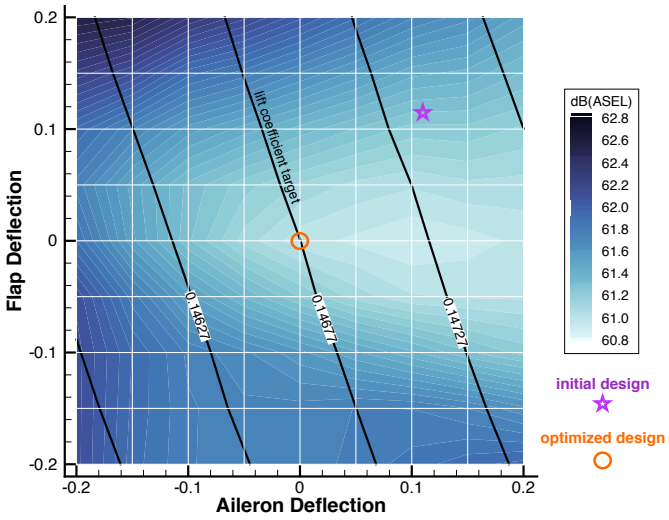


Fig. 27 Flood contours of *ASEL* with overlaid contour lines of lift coefficient in the flap-aileron design subspace. Note deflections are deviations from the optimized settings which is now at the origin.

At first glance, the color contours in Fig. 27 do not seem to indicate that the new design point is indeed an optimum in this subspace. An even better solution appears to exist with just a small increase in aileron deflection (to the right in Fig. 27). However, that evaluation does not account for the lift constraint. Fig. 27 also shows overlaid black contours lines of constant lift. When taking into account that the optimal solution must lie on the proper lift constraint contour line (which for this case is C_L = 0.14677), it becomes clear that the optimum of the problem has been located, at least in this subspace. This is further established in Fig. 28, where *ASEL* is plotted along this lift coefficient contour as a function of flap deflection. This plot confirms that the optimized point is indeed a local minimum in the flap-aileron design subspace.

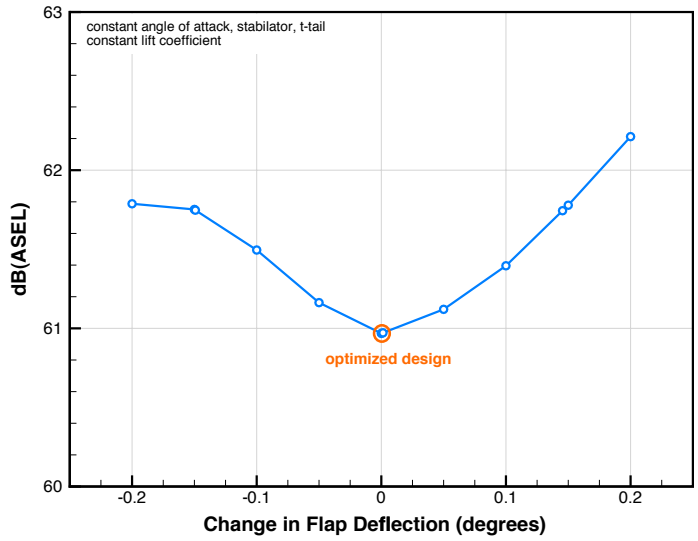


Fig. 28 *ASEL* variation at constant lift coefficient target in flap-aileron design subspace.

The stabilator is the largest control surface and therefore should have a significant effect on the aircraft sonic boom. Accordingly, design space surveys were also conducted in the flap-stabilator and aileron-stabilator subspaces. These design subspaces are presented in Fig. 29. Plots of *ASEL* along the cruise lift coefficient contour are presented in Fig. 30. These plots verify that the optimized design point is also a local minimum in the constrained flap-stabilator and aileron-stabilator design subspaces.

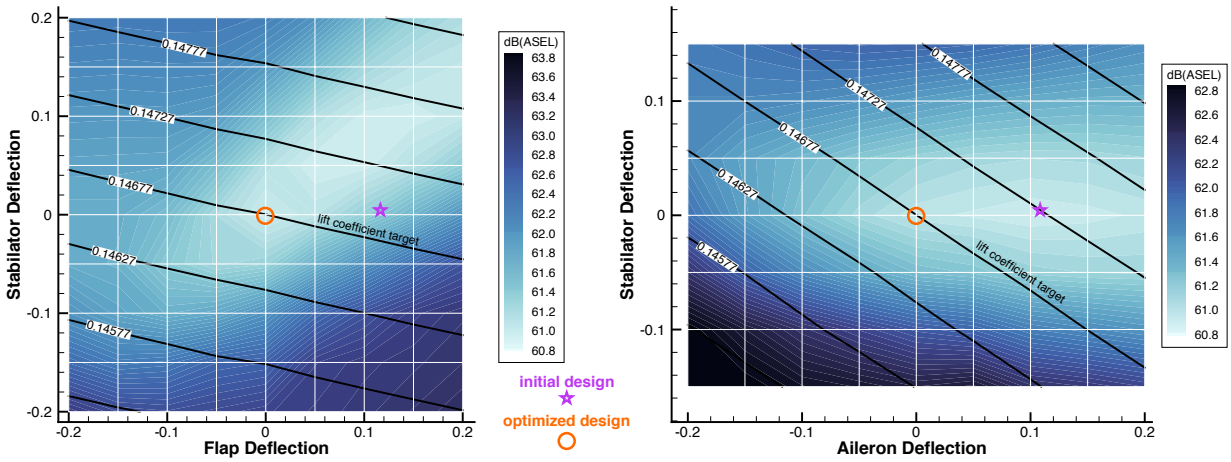


Fig. 29 Flood contours of *ASEL* with overlaid contour lines of lift coefficient in the flap-stabilator and aileron-stabilator design spaces subspace centered about the optimized design.

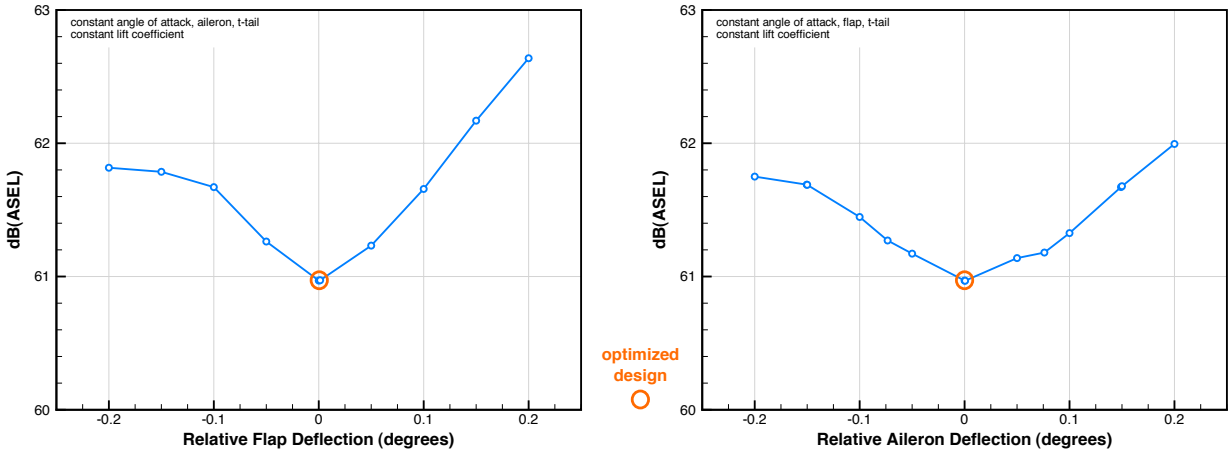


Fig. 30 ***ASEL*** **variation at constant lift in flap-stabilator and aileron-stabilator design subspaces.**

To assess the robustness of the design method, the optimization process was repeated with a different initial starting points in the design space. Based on the variations of the design variables as shown in Fig. 26, these repeat applications of the design method were conducted in reduced design spaces. In the first repeat optimization, the stabilator, T-tail, and angle of attack were held fixed to their optimal values. The second repeat run is identical except the angle of attack was allowed to vary. For both problems, the starting values of the aileron and flap deflections were quite different than for the original values as shown in Table 2.

Table 2 Initial deflections of control surfaces for repeat runs in reduced design spaces.

Control Surface	Minimum	Maximum	Initial
Ailerons	-3.0°	3.0°	0.79°
Flaps	-3.0°	3.0°	-1.72°

All optimization runs are mapped onto the aileron-flap subspace and presented in Fig. 31. The red curve is the projected trajectory of the original optimization as shown in Fig. 26. The magenta and orange curves show the trajectory of the repeat optimizations in the reduced design spaces. The magenta curve allowed only flap and aileron deflections to vary, while the orange did the same but added angle of attack as a variable. Note that the magenta and orange trajectories have a different initial starting point than the red trajectory. With the angle of attack allowed to vary, the orange trajectory takes a less direct path through the design space, but reaches essentially the same point at the end of the optimization. Also note that all three optimizations terminate in the same small area surrounding the optimum. These results demonstrate the repeatability of the optimization method.

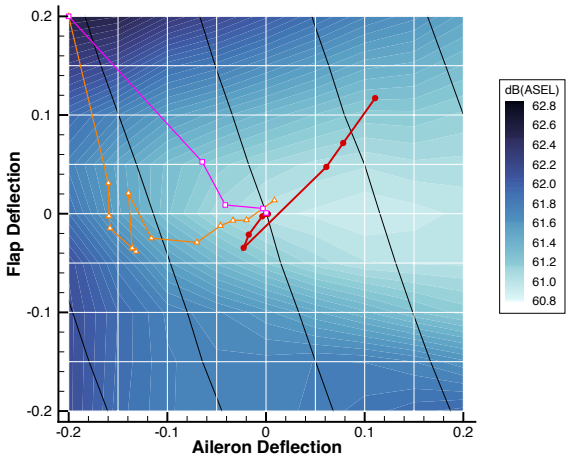


Fig. 31 Projection of three optimization trajectories in the aileron-flap deflection subspace. Red curve is original optimization with all variables active. Magenta curve is repeat optimization but only aileron and flap variables active. Orange curve had aileron, flap, and angle of attack variables active.

Fixed Lift and Trimmed

The typical X-59 mission will not require fixed altitude in the cruise segment, which means the lift *coefficient* is not really a hard constraint. Of course, for level flight with a specific payload and fuel load, the dimensional value of required lift is determined. Thus, to represent a more realistic design goal, a second optimization problem was set up where the altitude was allowed to float as summarized in Eq. (7):

$$\begin{aligned} &\text{minimize:} && ASEL\,(\alpha, \delta_f, \delta_a, \delta_s, \delta_t, h) \\ &\text{subject to:} && L\,(\alpha, \delta_f, \delta_a, \delta_s, \delta_t, h) = L_{cruise} \\ & && C_M(\alpha, \delta_f, \delta_a, \delta_s, \delta_t, h) = 0 \\ & && \delta_{f,min} \le \delta_f \le \delta_{f,max} \\ & && \delta_{a,min} \le \delta_a \le \delta_{a,max} \\ & && \delta_{s,min} \le \delta_s \le \delta_{s,max} \\ & && \delta_{t,min} \le \delta_t \le \delta_{t,max} \\ & && h_{min} \le h \le h_{max} \end{aligned} \tag{7}$$

Note that in addition to the constraint on lift, a pitching moment constraint is enforced to ensure trim, adding additional realism to the problem. Also note these deflections are always identical on each side of the airplane.

For this problem, significant changes in angle of attack were expected, and therefore the re-meshing technique used in the previous problem was not practical. Instead, the computational mesh is adapted for every analysis during the design process. The adaptation was driven by ground noise directly and thus fully utilized the coupled adjoint analysis capability. Using the design objective as the adaptation metric was also expected to improve accuracy of the both the objective and its gradients.

The version of the **sBOOM** tool used in this work (**v2.9.1**) does not provide gradients of the noise metrics with respect to altitude. Such a feature is under development, but until it is available, a model of the effects of altitude on ground-level noise has been created as a surrogate to close the design problem. Fig. 32 presents a plot of ground-level noise (*ASEL*) as a function of altitude for a fixed near-field pressure signature nearly identical to that produced by the X-59 at cruise. Note that the curve is nearly linear. This greatly simplifies the problem of the missing gradient of noise with respect to altitude. For this work, this gradient is assumed to be constant and hence the slope of a line fitted through the curve in Fig. 32. In practice, the altitude provided to **sBOOM** is fixed and then the computed ground-level loudness is adjusted for actual altitude using this constant gradient. This simple model should work for small changes to the design and flight conditions. However, when large changes to the pressure signature are expected, it is preferable to obtain these gradients directly from the atmospheric propagation code.

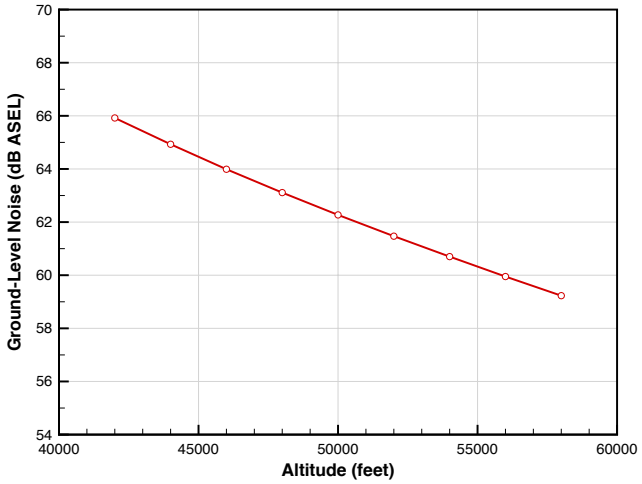


Fig. 32 Variation of *ASEL* ground-level noise metric as a function of altitude for a fixed near-field pressure signature.

One of the more current revisions (C612A) of the X-59 geometry was used for this optimization problem. As a reference, what is currently considered to be the best cruise flight condition (lowest ground noise) by the X-59 program is listed below in Table 3 as the nominal condition. Bounds for the deflections and altitude which stem from the vehicle's flight envelope are also provided. This represents the range of the design space that is considered in the optimizations presented below.

Table 3 Control surface deflection bounds and nominal values used in design optimization.

Design Variable	Nominal	Minimum	Maximum
Ailerons	1.1°	-3.0°	3.0°
Flaps	-2.4°	-3.0°	3.0°
Stabilator	3.42°	-15.0°	15.0°
T-tail	3.7°	0.0°	10.0°
Angle of Attack	2.09°	-	-
Altitude (feet)	53,200	52,000	54,000

Output-based mesh adaptation was used for all analyses generated on the aircraft in the design optimizations. Body-axis-aligned volume meshes with roughly 23 million cells were used to compute forces and moments on the full span of the aircraft. The aircraft forces were used as the functional for adapting these meshes. Stretched, Mach-wave-aligned adapted meshes ranging from 150-230 million cells were used to compute the near-field pressure signature three body lengths below the aircraft. These solutions were conducted using only half the span of the

airplane, thus exploiting a symmetry plane to conserve computational resources. The ground noise metric, *ASEL,* served as the adaptation functional. Note these meshes on the very complex X-59 are only roughly double the size of the meshes used with the very simple axisymmetric body. Even though these were only half-span meshes (full domain meshes were employed on the axisymmetric body), the X-59 meshes are relatively coarse when considering the complexity of the geometry. Coarser meshes were used due to constraints on computational resources and to avoid discovering unsteady flow features in the plume which can pollute and hinder the adjoint sensitivity calculation. Thus, some accuracy in the objective function and certainly the gradients was surrendered for this problem. Inaccurate gradients, of course, can hinder the optimization process.

Referring back to the nominal condition listed in Table 3, the coupled **`Cart3D-sBOOM`** analysis of this case in a standard atmosphere predicts an *ASEL* of 63.7 dBA. At this angle of attack and altitude (assuming a standard atmosphere), the aircraft generates the required lift for level flight and is very nearly trimmed. The first optimization attempted used this nominal condition as a starting point. The method immediately stalled and failed to find a better design condition. Either additional mesh refinement is needed to improve accuracy, or the nominal state is indeed in the region of a local minimum. Further exploration of the design space in the region would be necessary to verify either hypothesis. Establishing this state as a nominal baseline, two additional optimizations were completed with two different starting conditions. These are listed in Table 7. Notice that Case 1 is quite far from the nominal state, while Case 2 is much closer.

Table 4 Initial X-59 control surface deflection values.

Design Variable	Case 1	Case 2
Ailerons	0.0°	1.5°
Flaps	0.0°	-2.0°
Stabilator	3.0°	3.0°
T-tail	0.0°	4.0°
Angle of Attack	2.3°	2.25°
Altitude (feet)	53,200	53,200

The optimization results for Case 1 are summarized in Fig. 33. The initial condition was comparatively loud at almost 72 dBA and the aircraft was far from trimmed. After 6 design cycles, the ground noise has been reduced to 66.4 dBA, the lift matches the weight, and the aircraft is trimmed. This optimization stalled after the 6 design cycles and attempts to restart from this final design failed to find a better flight condition. Again, this could be due to one of

two reasons: either the design has reached a true local minimum, or additional mesh refinement is necessary to navigate the design space. Nevertheless, the optimizer was able to reduce ground noise over 5 decibels and achieve trimmed cruise. However, it was not able to produce a condition that was even at least as good as the nominal case which is still over 2 dBA quieter.

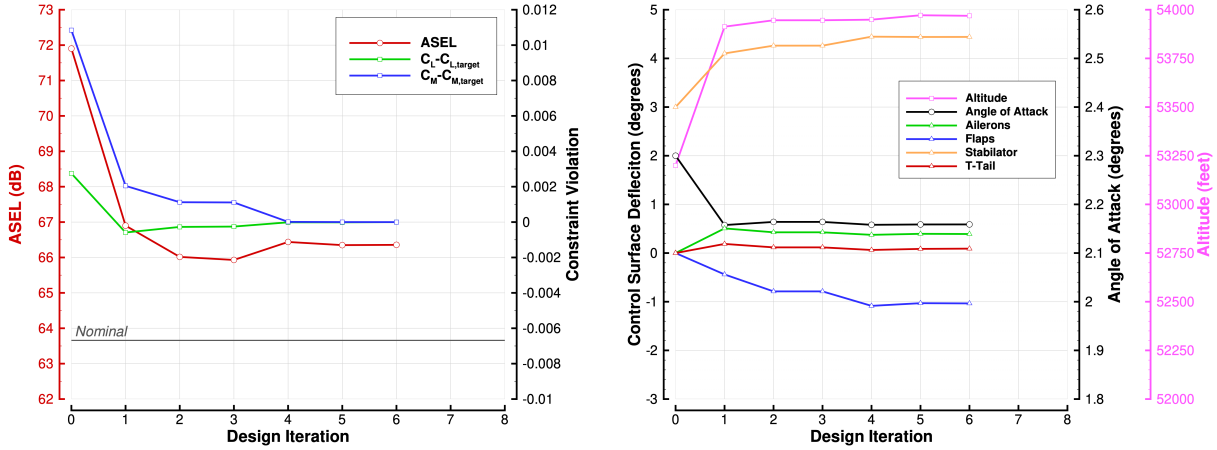


Fig. 33 Optimization history (Case 1) of X-59 with control surface deflections, altitude, and angle of attack as design variables. Objective (*ASEL*) and constraint violations (lift and moment) are shown on the left with the design variables on the right. The ground noise for the nominal case is also shown.

The ground signals for the initial, optimized, and nominal cases are shown in Fig. 34. The optimized signal shows a slightly lower peak up front due to the reduced angle of attack. But the major difference is the significant weakening of the rear shock which is the primary source of noise reduction. Comparing the optimized and nominal signatures reveals why the nominal case is still quieter. While the pressure jump for the aft shock is lower for the optimized case, the rise time of the nominal case is longer, which is the primary reason it is quieter.

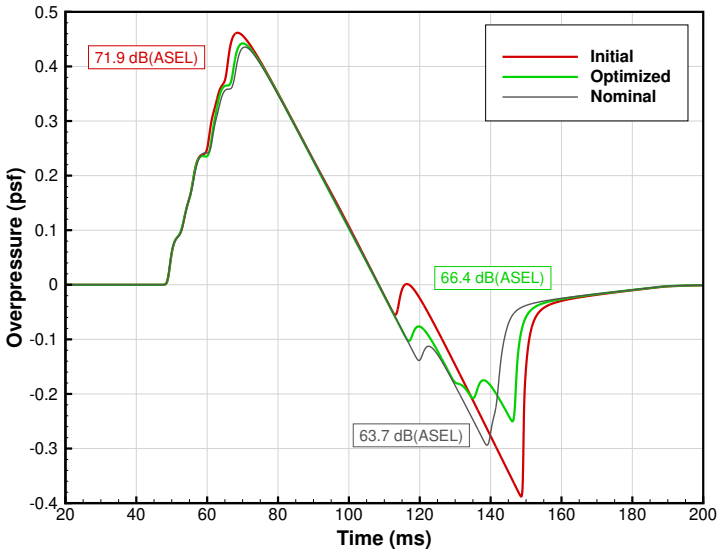


Fig. 34 Ground pressure signals from initial, optimized, and nominal conditions of the X-59 (Case 1).

The results for Case 2 which started much closer to the nominal condition are shown in Fig. 35. The initial condition is a little over 3 dBA louder than the nominal condition. The aircraft is also producing too much lift and is not trimmed. After 8 design cycles, the aircraft lift is now correct for cruise and the aircraft is trimmed. Also, the ground noise has been reduced to 63.4 dBA, which is a bit lower than that of the nominal condition. Looking at the ground signature comparison in Fig. 36, it is clear why. Both signatures are similar, particularly near the aft shock. However, the aft shock of the optimized signal is somewhat weaker. The slightly higher angle of attack of the optimized case produces a slightly higher peak of the front shock which should produce more noise. However, the optimized altitude has hit the maximum limit, which helps mitigate this increase in noise.

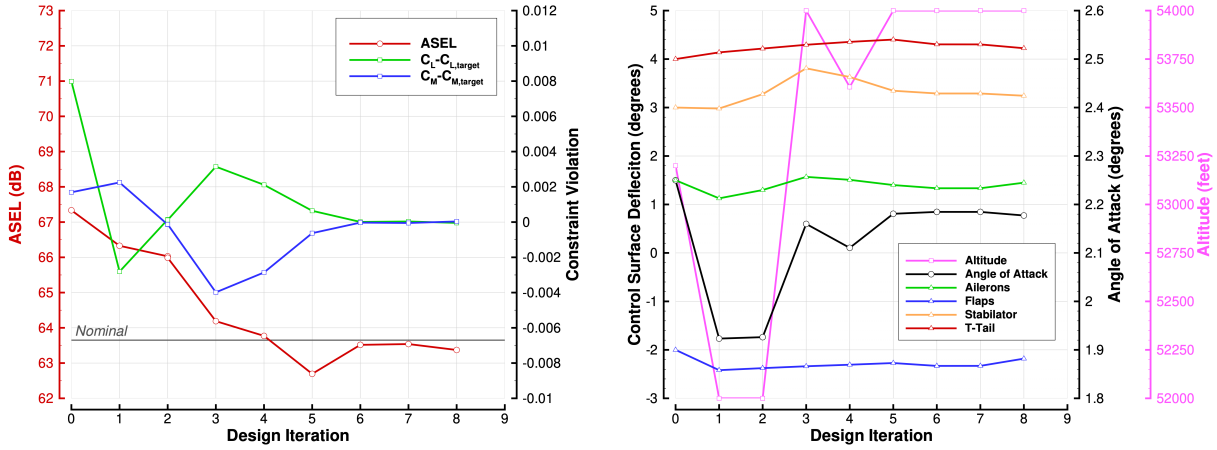


Fig. 35 Optimization history (Case 2) of X-59 with control surface deflections, altitude, and angle of attack as design variables. Objective (*ASEL*) and constraint violations (lift and moment) are shown on the left with the design variables on the right. The ground noise for the nominal case is also shown.

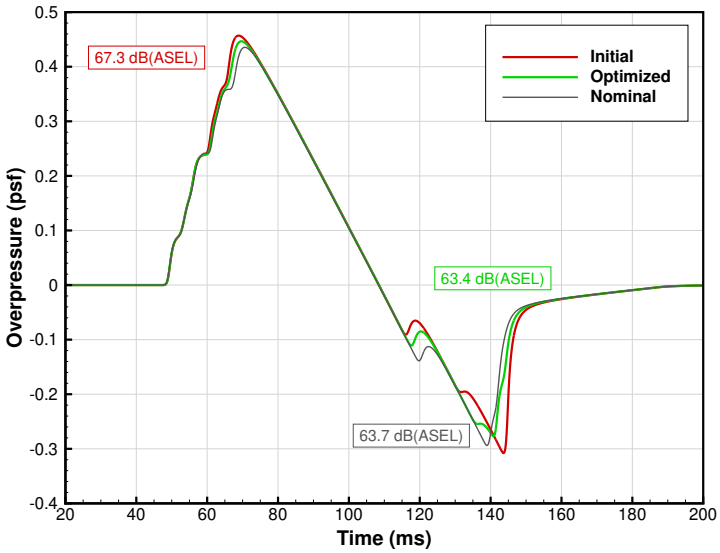


Fig. 36 Ground pressure signals from initial, optimized, and nominal conditions of the X-59 (Case 2).

The nominal and optimized conditions for both Case 1 and 2 are shown below in Table 5. Clearly the optimized Case 1 condition remains far from the nominal case, further suggesting a local minimum may have been located. Looking at Case 2, it is clear that all design variables (except the T-tail deflection) have moved closer to the nominal

condition from the initial state listed in Table 4. Note that even though deflections are listed to the hundredth of a degree, operationally it may not be possible to set some of these surfaces to that level of accuracy. However, the fact that both the nominal and optimized conditions result in similar ground noise suggests that they both may lie in a relatively flat region of the design space near a local minimum. Thus, these results bode well for the success of the X-59 program, as there likely is a reasonably sized region of the flight envelope that produces what has been identified as the lowest ground noise level so far.

Table 5 Optimized and nominal control surface deflection values for the X-59.

Design Variable	Nominal	Optimized (Case 1)	Optimized (Case 2)
Ailerons	1.1°	0.39°	1.44°
Flaps	-2.4°	-1.03°	-2.18°
Stabilator	3.42°	4.44°	3.24°
T-tail	3.7°	0.09°	4.22°
Angle of Attack	2.09°	2.16°	2.18°
Altitude (feet)	53,200	53,969	54,000

Maximize Noise at Fixed Altitude

The X-59 project presented the authors with an interesting problem. The flight test program wishes to fly a much louder aircraft over the test range to obtain wide bounds for the noise metrics, thus enhancing statistical significance of the survey results. Rather than fly a second (louder) airplane, the program sought to identify a feasible flight condition that would *maximize* the ground-level noise of the X-59. Limited time was given to solve the problem so a much louder flight condition was manually identified through trial and error tempered by basic engineering knowledge. However, as the noise-driven design optimization process became available, it was used to verify that the maximum noise condition had indeed been discovered. The results of this work are presented here.

The manually identified condition for maximum noise is detailed in Table 6. This aircraft configuration and flight condition produces a ground-level noise of 77.9 dB (*ASEL)*. To verify this was a maximum noise condition, the design optimization method was applied to the aircraft at fixed altitude and Mach number. All control surface deflections and the angle of attack were allowed to vary.

Table 6 Flight condition and control surface deflection values for maximum ground noise.

Ailerons	4.0°
Flaps	4.0°
Stabilator	0.82°
T-tail	3.7°
Mach number	1.3
Angle of attack	1.02°
Altitude	43,000 feet

The control surface initial conditions of this optimization are given in Table 7 along with the bounds. Note that they are quite different than the deflections given in Table 6. The objective was to maximize *ASEL* while maintaining trimmed, cruise lift at Mach 1.3 at an altitude of 43,000 feet, which is near the bottom of the operating envelope at this speed. This optimization problem is summarized in Eq. (8):

$$\begin{aligned} \text{maximize:} \quad & ASEL\,(\alpha, \delta_f, \delta_a, \delta_s, \delta_t) \\ \text{subject to:} \quad & C_L\,(\alpha, \delta_f, \delta_a, \delta_s, \delta_t) = C_{L,cruise} \\ & C_M(\alpha, \delta_f, \delta_a, \delta_s, \delta_t) = 0 \\ & \delta_{f,min} \le \delta_f \le \delta_{f,max} \\ & \delta_{a,min} \le \delta_a \le \delta_{a,max} \\ & \delta_{s,min} \le \delta_s \le \delta_{s,max} \\ & \delta_{t,min} \le \delta_t \le \delta_{t,max} \end{aligned} \tag{8}$$

For this problem, output-based mesh adaptation was used for every mesh generated on the full aircraft since angle of attack was expected to vary significantly. A body-axis-aligned volume mesh with roughly 22 million cells was used to compute forces and moments. A stretched, Mach-angle-aligned mesh with about 33 million cells was used to compute the near-field pressure signature.

Table 7 Control surface deflection bounds and initial values in design optimization.

Design Variable	Minimum	Maximum	Initial
Ailerons	-3.0°	4.0°	2.0°
Flaps	-3.0°	4.0°	2.0°
Stabilator	-15.0°	15.0°	0.0°
T-tail	0.0°	10.0°	5.0°

The results of this optimization are shown in Fig. 37. Note that the final solution is essentially the same as that in Table 6 except for a slight change in the stabilator and T-tail deflections. The optimizer was able to find a slightly higher noise (78.0 dB (*ASEL*)) configuration but mostly verified a maximum noise case had been identified. The flap and aileron deflections hit the maximum bound values. Angle of attack and stabilator values were mostly driven by the lift and moment constraints. The T-tail did deflect a bit more to relieve the stabilator's need to trim the aircraft, but overall the T-tail's influence was very small. Overall, the variations in the control surfaces from the starting point were significant; both the flaps and ailerons deflected two more degrees hitting their upper bounds. Angle of attack varied over half a degree. The noise was increased by three full decibels while attaining level trimmed flight. This was definitely a successful application of the design method.

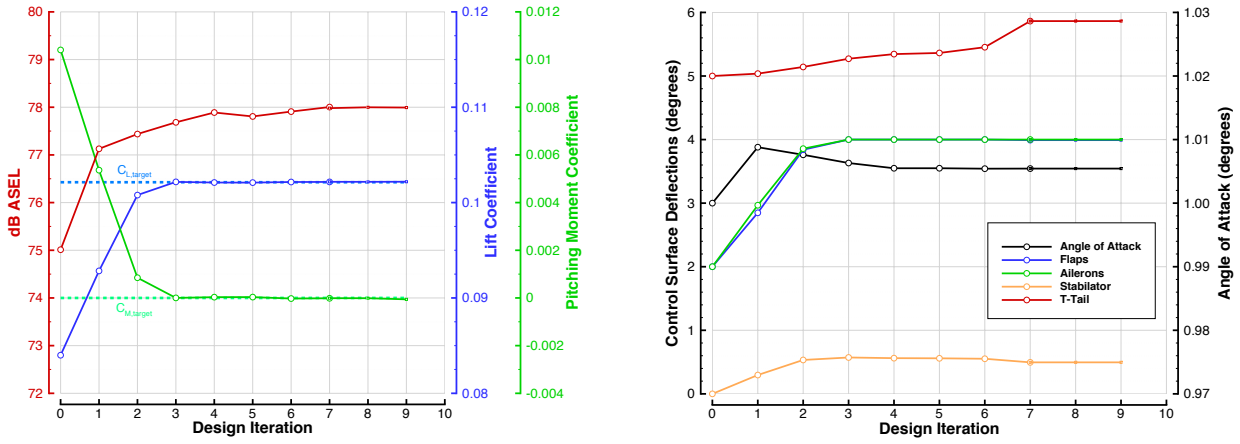


Fig. 37 Optimization history of objective (*ASEL*) and constraints (lift and pitching moment coefficients) in the left plot for ground-level noise maximization problem. Variation of control surface deflections and angle of attack in the right plot.

IV. Conclusions

A multidisciplinary design optimization tool that directly minimizes ground-level noise from supersonic aircraft has been presented. The method successfully couples a Cartesian Euler flow solver with an atmospheric propagation tool with built-in noise metric calculation. Adjoint solvers for both the flow solver and propagation tool have proven to be enabling technologies. The coupled adjoint solver has been successfully applied to output-based mesh adaptation where the functional of interest is the ground-level noise itself. This allows for more accurate computation of not only the noise level, but also any desired sensitivities. Using the coupled adjoint solver to compute ground noise sensitivities to user-defined design variables allows for gradient-based design optimization and thus direct minimization of ground noise.

The design method has been successfully applied to two geometries. The first was a simple axisymmetric body that is built with a limited number of design parameters. This problem allowed for sufficiently large computational meshes which produced very accurate noise estimates and gradients. These gradients were verified by locally sampling the nearby design space. Further sampling revealed that even with a limited number of design parameters, the design space was smooth albeit multimodal. Optimizations were performed using starting points within each basin of attraction to demonstrate reliable convergence to each local minimum. This was demonstrated by graphically projecting the optimization trajectories onto the sampled design space.

The second geometry was an actual low-boom aircraft design. The control surface deflections and flight condition were optimized to minimize the ground noise of the aircraft. Three design problems were completed on this aircraft. The first and simplest problem minimized ground noise at fixed altitude and lift. This simpler problem facilitated in depth design space analysis to verify a local minimum was indeed discovered. The second design problem included constraints on lift (for level, unaccelerated flight) and pitching moment to maintain trim. Two results were presented with different starting points, producing two different optimized ground noise values. The first result showed a reduction of over 5 decibels starting from a loud initial condition. The second result had a quieter initial state but was able to reduce the ground noise over 3 decibels. These results suggest this design space is also multimodal. The lower of the two noise values was very close to what was previously considered the lowest noise possible. While it has not been shown this is the global optimum, successfully achieving the best previously

known value further demonstrates the capability of the design method. The final design problem was a noise maximization problem, which successfully discovered the a priori known solution within the design variable bounds.

Taken together, the results show excellent gradient accuracy and reliable search directions even in problems with elaborate geometry and complex signatures with many shocks. Moreover, the optimizations demonstrate the importance of solving the fully coupled problem and highlight the pitfalls of nearfield inverse design. The capability to make relatively minor adjustments to an aircraft's control surface settings to minimize noise on the ground after a propagation of over twenty kilometers through the atmosphere has several practical applications. For example, it should be possible to make accurate predictions of X-59 test flight settings that fine tune noise exposure to the ground.

V. Future Work

The results from all of the optimization problems presented strongly suggest that for any parametrized complex or even simple geometry, the ground-noise design space is likely multimodal. Successfully locating a global optimum is likely to require hybrid optimization strategies, thus involving global optimization techniques (e.g., genetic algorithms) along with local gradient-based minimization. Such techniques will also be necessary should the design method ever be applied in a conceptual design setting.

Acknowledgements

This research was supported by the NASA ARMD Commercial Supersonic Technology (CST) Project and by NASA Ames Research Center contract NNA16BD60C. Computing resources supporting this work were provided by the NASA High-End Computing (HEC) Program through the NASA Advanced Supercomputing (NAS) Division at Ames Research Center. Finally, the authors would also like to recognize that George Anderson performed some of the initial studies of this work.

References

[1] Carter, M., Campbell, R., and Nayani, S., "USM3D Analysis of Low Boom Configuration," AIAA Paper 2011-3335, June 2011. doi:10.2514/6.2011-3335

[2] Choi, S., Alonso, J. J., and Van der Weide, E., "Numerical and Mesh Resolution Requirements for Accurate Sonic Boom Prediction," *Journal of Aircraft*, Vol. 46, No. 4 (2009), pp. 1126-1139. doi:10.2514/1.34367

[3] Cliff, S. E., Thomas, S. D., McMullen, M. S., and Melton, J. E., "Assessment of Unstructured Euler Methods for Sonic Boom Pressure Signatures Using Grid Refinement and Domain Rotation Methods," NASA TM 2008-214568, Sept. 2008.

[4] Cliff, S. E., Elmiligui, A., and Campbell, R., "Evaluation of Refined Tetrahedral Meshes With Projected, Stretched, and Sheared Prism Layers for Sonic Boom Analysis," AIAA Paper 2011-3338, June 2011. doi:10.2514/6.2011-3338

[5] Howe, D., "Hybrid Cart3D/OVERFLOW Near-Field Analysis of a Low Boom Configuration With Wind Tunnel Comparisons," AIAA Paper 2011-3336, June 2011. doi:10.2514/6.2011-3336

[6] Park, M. A. and Nemec, M., "Nearfield Summary and Statistical Analysis of the Second AIAA Sonic Boom Prediction Workshop," *Journal of Aircraft*, Vol. 56, No. 3 (2019), pp. 851-875. doi:10.2514/1.C034866

[7] Park, M., "Low Boom Configuration Analysis With FUN3D Adjoint Simulation Framework," AIAA Paper 2011-3337, June 2011. doi:10.2514/6.2011-3337

[8] Wintzer, M., Nemec, M., and Aftosmis, M. J., "Adjoint-Based Adaptive Mesh Refinement for Sonic Boom Prediction," AIAA Paper 2008-6593, Aug. 2008. doi:10.2514/6.2008-6593

[9] Plotkin, K. J. and Grandi, F., "Computer Models for Sonic Boom Analysis: PCBoom4, CABoom, BooMap, CORBoom," *Wyle Report WR* 211, 2002.

[10] Rallabhandi, S. K., "Advanced Sonic Boom Prediction Using the Augmented Burgers Equation," *Journal of Aircraft*, Vol. 48, No. 4 (2011), pp. 1245-1253. doi:10.2514/1.C031248

[11] Thomas, C. L., "Extrapolation of Sonic Boom Pressure Signatures By the Waveform Parameter Method," NASA TN D-6832, 1972.

[12] Rallabhandi, S. K. and Loubeau, A., "Summary of Propagation Cases of the Second AIAA Sonic Boom Prediction Workshop," *Journal of Aircraft*, Vol. 56, No. 3 (2018), pp. 876-895. doi:10.2514/1.C034805

[13] Rallabhandi, S. K. and Loubeau, A., "Summary of Propagation Cases of the Third AIAA Sonic Boom Prediction Workshop," *Journal of Aircraft*, (2021), pp. 1-17. doi:10.2514/1.c036327

[14] Aftosmis, M. J., Nemec, M., and Cliff, S. E., "Adjoint-Based Low-Boom Design With Cart3D," AIAA Paper 2011-3500, June 2011. doi:10.2514/6.2011-3500

[15] Li, W. and Rallabhandi, S., "Inverse Design of Low-Boom Supersonic Concepts Using Reversed Equivalent-Area Targets," *Journal of Aircraft*, Vol. 51, No. 1 (2014), pp. 29-36. doi:10.2514/1.C031551

[16] Nadarajah, S., Jameson, A., and Alonso, J., "Sonic Boom Reduction Using an Adjoint Method for Wing-Body Configurations in Supersonic Flow," AIAA Paper 2002-5547, Sept. 2002. doi:10.2514/6.2002-5547

[17] Rallabhandi, S. K. and Mavris, D. N., "Sonic Boom Minimization Using Inverse Design and Probabilistic Acoustic Propagation," *Journal of Aircraft*, Vol. 43, No. 6 (2006), pp. 1815-1828. doi:10.2514/1.20457

[18] Wintzer, M. and Kroo, I. M., "Optimization and Adjoint-Based CFD for the Conceptual Design of Low Sonic Boom Aircraft," AIAA Paper 2012-0963, 2012. doi:10.2514/6.2012-963

[19] Rallabhandi, S. K., Nielsen, E. J., and Diskin, B., "Sonic-Boom Mitigation Through Aircraft Design and Adjoint Methodology," *Journal of Aircraft*, Vol. 51, No. 2 (2014), pp. 502-510. doi:10.2514/1.C032189

[20] NASA, "Low Boom Flight Demonstration Overview," Aug. 2019. URL: https://www.nasa.gov/mission_pages/lowboom/overview.

[21] Haimes, R. and Dannenhoffer, J., "The Engineering Sketch Pad: A Solid-Modeling, Feature-Based, Web-Enabled System for Building Parametric Geometry," AIAA Paper 2013-3073, 2013. doi:10.2514/6.2013-3073

[22] Dannenhoffer, J., "OpenCSM: An Open-Source Constructive Solid Modeler for MDAO," AIAA Paper 2013-701, 2013. doi:10.2514/6.2013-701

[23] Haimes, R. and Aftosmis, M., "On Generating High-Quality Water-Tight Triangulations Directly From CAD," *Proceedings of the International Society for Grid Generation (ISGG)*, 2002.

[24] Dannenhoffer, J. and Haimes, R., "Using Design-Parameter Sensitivities in Adjoint-Based Design Environments," AIAA Paper 2017-0139, 2017. doi:10.2514/6.2017-0139

[25] Aftosmis, M. J., Berger, M. J., and Adomavicius, G., "A Parallel Multilevel Method for Adaptively Refined Cartesian Grids With Embedded Boundaries," AIAA Paper 2000-0808, Jan. 2000. doi:10.2514/6.2000-808

[26] Aftosmis, M. J., Berger, M. J., and Melton, J. E., "Robust and Efficient Cartesian Mesh Generation for Component-Based Geometry," *AIAA Journal*, Vol. 36, No. 6 (1998), pp. 952-960. doi:10.2514/2.464

[27] Nemec, M., Aftosmis, M., Murman, S., and Pulliam, T., "Adjoint Formulation for an Embedded-Boundary Cartesian Method," AIAA Paper 2005-877, Jan. 2005. doi:10.2514/6.2005-877

[28] Nemec, M. and Aftosmis, M., "Adjoint Error Estimation and Adaptive Refinement for Embedded-Boundary Cartesian Meshes," AIAA Paper 2007-4187, June 2007. doi:10.2514/6.2007-4187

[29] Nemec, M. and Aftosmis, M. J., "Adjoint Sensitivity Computations for an Embedded-Boundary Cartesian Mesh Method," *Journal of Computational Physics*, Vol. 227, No. 4 (2008), pp. 2724-2742. doi:10.1016/j.jcp.2007.11.018

[30] Aftosmis, M. J. and Nemec, M., "Cart3D Simulations for the First AIAA Sonic Boom Prediction Workshop," AIAA Paper 2014-0558, Jan. 2014. doi:10.2514/6.2014-0558

[31] Anderson, G. R., Aftosmis, M. J., and Nemec, M., "Cart3D Simulations for the Second AIAA Sonic Boom Prediction Workshop," *Journal of Aircraft*, Vol. 56, No. 3 (2019), pp. 896-911. doi:10.2514/1.C034842

[32] Rallabhandi, S., "Sonic Boom Adjoint Methodology and Its Applications," AIAA Paper 2011-3497, June 2011. doi:10.2514/6.2011-3497

[33] Meyer-Bisch, C., "Measuring Noise," *Medecine Sciences: M/S*, Vol. 21, No. 5 (2005), pp. 546-550. doi:10.1051/medsci/2005215546

[34] Rallabhandi, S. K. and Park, M. A., "Adjoint-Based Mesh Adaptation for the Sonic Boom Signature Loudness," AIAA Paper 2017-3049, June 2017. doi:10.2514/6.2017-3049

[35] Stevens, S. S., "Perceived Level of Noise By Mark VII and Decibels (E)," *The Journal of the Acoustical Society of America*, Vol. 51, No. 2B (February 1972), pp. 575-601. doi:abs/10.1121/1.1912880

[36] Gill, P. E., Murray, W., and Saunders, M. A., "SNOPT: An SQP Algorithm for Large-Scale Constrained Optimization," *SIAM Review*, Vol. 47, No. 1 (2005), pp. 99-131. doi:10.1137/S0036144504446096

[37] Nemec, M., Aftosmis, M. J., Rallabhandi, S. K., and Rodriguez, D. L., "Goal-Oriented Discretization Error Control in Coupled Nearfield-Farfield Low-Boom Simulations," AIAA Paper 2022-4085, June 2022. doi:10.2514/6.2022-4085

[38] Nemec, M. and Aftosmis, M., "Parallel Adjoint Framework for Aerodynamic Shape Optimization of Component-Based Geometry," AIAA Paper 2011-1249, Jan. 2011. doi:10.2514/6.2011-1249

[39] Durston, D. A., Elmiligui, A. A., Cliff, S. E., Winski, C., Carter, M. B., and Walker, E., "Experimental and Computational Sonic Boom Assessment of Boeing N+2 Low Boom Models," AIAA Paper 2014-2140, June 2014. doi:10.2514/6.2014-2140